Density Estimation for Dynamic Volumes

Christian Fuchs[+] Tongbo Chen[+] Michael Goesele[*]
Holger Theisel[†] Hans-Peter Seidel[+]

MPI Informatik[+] *University of Washington*[*] *University of Bielefeld*[†]

Abstract

We propose a new approach to capture the volumetric density of dynamic scattering media instantaneously with a single image. The volume is probed with a set of laser lines and the scattered intensity is recorded by a conventional camera. We then determine the density along the laser lines taking the scattering properties of the media into account. A specialized approximation technique reconstructs the full density field in the volume. We apply the technique to capture the volumetric density of participating media such as smoke.

Key words: Computer Graphics, Picture/Image Generation — Digitizing and Scanning, Computational Geometry and Object Modeling — Physically Based Modeling

1. Introduction and Previous Work

The acquisition of time-varying volumetric density fields has recently attracted the attention of computer graphics researchers. Hasinoff and Kutulakos [1] presented a multi-view method to volumetrically reconstruct flames using a photo-consistency approach. Ihrke and Magnor [2, 3] used sparse view tomography to reconstruct flames and optically thin smoke from a small set of camera views. Hawkins et al. [4] captured time-varying smoke density by rapidly scanning a laser plane through a volume and imaging the light scattered by individual smoke particles from a lateral view with a high-speed camera (see Figure 1, left). This allows them to sample locations in the moving light plane with high spatial resolution yielding high quality renderings of the captured model. Physical measurement systems such as Yip et al. [5] or laser induced fluorescence (LIF) [6] follow a similar approach and capture the whole volume *sequentially* from a single view.

Our method is inspired by single view techniques but takes a fundamentally different sampling approach: The volume is illuminated with a grid of laser lines in order to sample the whole volume *simultaneously.* Essentially, the 2D laser plane is discretized and spread out to discrete locations in space. The volume is captured with a standard camera. As illustrated in Figure 1, this trades (potentially) continuous sampling in one spatial domain (Δy) against continuous sampling in the time domain (Δt). Careful placement of camera and light sources avoids occlusions when the laser lines are projected onto the image plane and the full but sparser sampled 3D information is captured with a single image. The sampling density can be increased by projecting multiple grids of differently colored illumination into the volume.

This new sampling paradigm has several consequences:

Decoupling of spatial and temporal sampling: The system captures the volume with a single camera image. It therefore enables continuous sampling in the time domain allowing both integration over long time intervals for weak signals and extremely short acquisition times for fast-changing datasets.

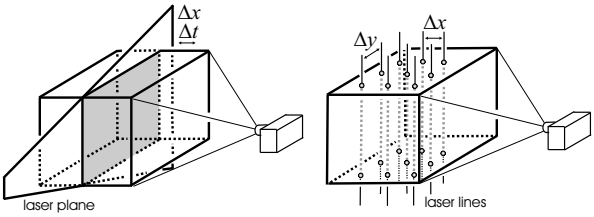

Fig. 1. Different acquisition approaches. *Left:* Sequential scanning of the volume with a plane of light as implemented by Hawkins et al. [4] with discrete sampling in time (Δt) and one spatial dimension (Δx). *Right:* New approach with simultaneous capture of volume density using line grids as illumination and discrete sampling in two spatial dimensions ($\Delta x, \Delta y$).

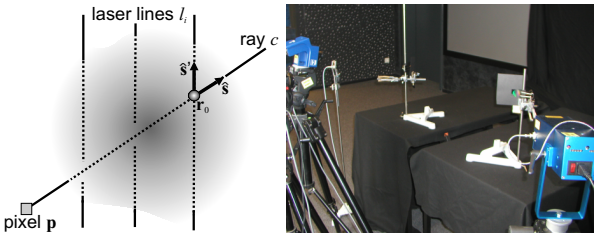

Fig. 2. *Left:* Situation for an individual ray c. *Right:* Image of the actual acquisition setup with camera on the left and two laser sources (left near camera and blue box on the right). When active, smoke is generated between the two tables.

Increased time resolution: Using the same camera hardware, frame rates can be increased by 1–2 orders of magnitude. Furthermore, the system contains no mechanically moving parts, i.e., the achievable time resolution is only limited by the imaging hardware and the illumination intensity.

Limited spatial resolution: Spatial resolution is fundamentally limited by the number of laser lines that can be resolved by the imaging system. Sampling is denser along the direction of the laser lines but spatial detail between sampling lines is lost, resulting in potential aliasing.

Density instead of photo-consistency: The actual density of scatterers is reconstructed (up to a scale factor) instead of a photo-consistent representation of the volume as in Hasinoff and Kutulakos [1].

In the remainder of the paper we first describe the basic concepts underlying our capture approach (Section 2). We then analyze its properties and study the resulting errors using a synthetic smoke dataset (Section 3). We describe our prototypical acquisition system and show results for real captured datasets (Section 4). The paper concludes with a discussion (Section 5) and future work (Section 6).

2. System Description

Figure 1, right, gives an overview over the measurement setup. We assume that the measurement volume contains a spatially varying density of scattering particles that we would like to measure. Apart from their density, the scattering properties of the individual particles should be constant (or be well approximated by a constant). Depending on the size of the particles, scattering will either be dominated by Mie scattering (for larger particles such as typically found in smoke) or by Raleigh scattering [7]. In the remainder of this section, we first describe the principles of radiative transfer (Section 2.1) and develop our image formation model (Section 2.2). Section 2.3 shows how we can recover the density of scatterers along the laser lines illuminating the volume. We finally describe in Section 2.4 how we can recover the full density field from this information.

2.1. *Radiative Transfer*

We start our analysis with the equation of radiative transfer [8] which describes the change in specific intensity $I(\mathbf{r},\hat{\mathbf{s}})$ [1] for a small volume element ds at a position $\mathbf{r}$ in space and in a direction $\hat{\mathbf{s}}$:

$$\frac{dI(\mathbf{r},\hat{\mathbf{s}})}{ds} = -\rho\sigma_t I(\mathbf{r},\hat{\mathbf{s}}) + \frac{\rho\sigma_t}{4\pi}\int_{4\pi} p(\hat{\mathbf{s}},\hat{\mathbf{s}}')I(\mathbf{r},\hat{\mathbf{s}}')d\omega' + \varepsilon(\mathbf{r},\hat{\mathbf{s}}). \quad (1)$$

The first term models a decrease in specific intensity due to absorption and outscattering which is proportional to the number of particles per unit volume ρ and the extinction cross section σ_t. The second term describes the increase in specific intensity due to inscattering which depends additionally on the phase function $p(\hat{\mathbf{s}},\hat{\mathbf{s}}')$. $\varepsilon(\mathbf{r},\hat{\mathbf{s}})$ is the emission from within ds.

In our measurement system (see Figure 1, right, and Figure 2 for the principle of the approach and the notation) we assume that light is scattered from homogeneous particles inside the volume. The extinction cross section σ_t and the phase function $p(\hat{\mathbf{s}},\hat{\mathbf{s}}')$ are constant throughout the volume but the number of particles per unit volume $\rho = \rho(\mathbf{r})$ varies. We furthermore assume that the laser lines l_i are generated outside the observation volume so that there is no emission inside, i.e.,

[1] Note that specific intensity can be converted into radiance by integrating over the spectrum of the radiation.

$\varepsilon(\mathbf{r},\hat{\mathbf{s}}) = 0$. The goal of the measurements is to recover $\rho(\mathbf{r})$ up to a scale factor, i.e., it is sufficient to recover $D(\mathbf{r}) = \sigma_t \rho(\mathbf{r})$. Equation 1 simplifies then to the first order differential equation

$$\frac{dI(\mathbf{r},\hat{\mathbf{s}})}{ds} = -D(\mathbf{r})I(\mathbf{r},\hat{\mathbf{s}}) + \frac{D(\mathbf{r})}{4\pi}\int_{4\pi} p(\hat{\mathbf{s}},\hat{\mathbf{s}}')I(\mathbf{r},\hat{\mathbf{s}}')d\omega'. \quad (2)$$

which we would like to solve under the boundary conditions given by our setup and assumptions.

2.2. *Image Formation Model*

We now take the specific situation of our measurement setup into account: The incident intensity I_i at a position $\mathbf{r}_0$ where the backprojected ray c of a pixel $\mathbf{p}$ with direction $-\hat{\mathbf{s}}$ intersects with a laser line l_i with direction $\hat{\mathbf{s}}_{l_i}$ can be computed as

$$I_i(\mathbf{r}_0,\hat{\mathbf{s}}) = \frac{D(\mathbf{r}_0)}{4\pi} I_{l_i}(\mathbf{r}_0,\hat{\mathbf{s}}_{l_i}) p(\hat{\mathbf{s}},\hat{\mathbf{s}}_{l_i}). \quad (3)$$

This is, however, only valid if $\mathbf{p}$ covers the full width of the laser line l_i. We will show in Section 4.1 how we lift this restriction in practice.

We assume in the following that $I_{l_i}(\mathbf{r}_0,\hat{\mathbf{s}}_{l_i}) = I_{l_i}$ is constant along each laser line l_i and can be calibrated in a separate step. Following Ishimaru [8] we can now split the intensity along the ray c into two terms:

$$I(\mathbf{r},\hat{\mathbf{s}}) = I_{\mathrm{ri}}(\mathbf{r},\hat{\mathbf{s}}) + I_{\mathrm{d}}(\mathbf{r},\hat{\mathbf{s}}). \quad (4)$$

The reduced intensity $I_{\mathrm{ri}}(\mathbf{r},\hat{\mathbf{s}})$ models the decay of I_i due to absorption and outscattering along c according to the first term in Equation 2:

$$I_{\mathrm{ri}}(s) = I_i(\mathbf{r}_0,\hat{\mathbf{s}})e^{-\tau} = I_i(\mathbf{r}_0,\hat{\mathbf{s}})e^{-\int_0^s D(\mathbf{r})ds}. \quad (5)$$

s measures the distance from $\mathbf{r}_0$ along the ray c to the pixel $\mathbf{p}$. Note that unlike [8], we treat $I_i(\mathbf{r}_0,\hat{\mathbf{s}})$ as a radiation source inside the volume. The remaining contributions caused by inscattering from the volume are accumulated in the diffuse intensity $I_{\mathrm{d}}(\mathbf{r},\hat{\mathbf{s}})$. The specific intensity that reaches pixel $\mathbf{p}$ can therefore be described as:

$$I_{\mathbf{p}} = I_{\mathrm{ri}}(s) + I_{\mathrm{d}}(s). \quad (6)$$

2.3. *Recovering $D(\mathbf{r})$ along Laser Lines l_i*

The goal of this section is to recover the scaled density values $D(\mathbf{r})$ along the laser lines l_i. We rewrite Equation 6 using Equations 3 and 5:

$$I_{\mathbf{p}} = \frac{D(\mathbf{r}_0)}{4\pi} I_{l_i} p(\hat{\mathbf{s}},\hat{\mathbf{s}}_{l_i}) e^{-\int_0^s D(\mathbf{r})ds} + I_{\mathrm{d}}(s). \quad (7)$$

This can be rewritten as

$$D(\mathbf{r}_0) = 4\pi \frac{I_{\mathbf{p}} - I_{\mathrm{d}}(s)}{I_{l_i} p(\hat{\mathbf{s}},\hat{\mathbf{s}}_{l_i})} \cdot e^{\int_0^s D(\mathbf{r})ds}. \quad (8)$$

The phase function $p(\hat{\mathbf{s}},\hat{\mathbf{s}}')$ can either be assumed to be isotropic, theoretically derived from the properties of the scattering media [7], or be measured experimentally [4]. Note, however, that our acquisition setup evaluates $p(\hat{\mathbf{s}},\hat{\mathbf{s}}')$ only over a small range of angles (all possible intersection angles of a laser line l_i and a ray c in Figure 2). Locally approximating $p(\hat{\mathbf{s}},\hat{\mathbf{s}}')$ with a constant yields therefore only a small error. The error can be minimized by placing the camera far away from the scene in order to approximate an orthographic projection. I_{l_i} can be determined in a calibration step for each laser line l_i.

The diffuse intensity $I_{\mathrm{d}}(s)$ can be estimated from the set of camera pixels $N(\mathbf{p})$ in the spatial neighborhood of $\mathbf{p}$ whose backprojected ray does not intersect with any laser line l_i:

$$I_{\mathrm{d}}(s) \approx \tilde{I}_{\mathrm{d}}(s) = \frac{1}{||N(\mathbf{p})||} \sum_{\mathbf{p}' \in N(\mathbf{p})} I_{\mathbf{p}'}. \quad (9)$$

This assumes that $I_{\mathrm{d}}(s)$ varies smoothly over the image plane and corresponds to the removal of multiple scattering in the calibration part of Hawkins et al. [4]. We furthermore need to set $\tilde{I}_{\mathrm{d}}(s) = I_{\mathbf{p}}$ if $\tilde{I}_{\mathrm{d}}(s) > I_{\mathbf{p}}$ to avoid physically implausible results, e.g., due to noise in the acquisition. Under the assumption of optically thin scattering material, we can furthermore set $\int_0^s D(\mathbf{r})ds = 0$ without introducing a too large error. Equation 8 then becomes

$$D(\mathbf{r}_0) \approx 4\pi \frac{I_{\mathbf{p}} - \tilde{I}_{\mathrm{d}}(s)}{I_{l_i} p(\hat{\mathbf{s}},\hat{\mathbf{s}}_{l_i})} \quad (10)$$

which allows us to recover the scaled density values along all laser lines.

2.4. *Reconstruction of the Entire Density Field $D(\mathbf{r})$*

The previous section introduced an approach to capture D along the laser lines. We will now discuss both interpolation and approximation approaches to recover $D(\mathbf{r})$ from this information.

2.4.1. *Interpolation*

Given the density values D along the laser lines, we can employ an interpolation technique to interpolate $D(\mathbf{r})$. The push-pull algorithm [9,10], for example, fills in missing parts in an image by iterative downsampling and upsampling of the image using a filter kernel at multiple resolutions. It can be easily generalized from 2D image data to 3D volume data.

The push-pull algorithm is able to fill in large missing parts at coarse resolution levels while it approximates the high-frequency detail at the finer levels. Before each iteration, the known values are reintroduced into the image resp. volume thus making the push-pull algorithm an interpolation method that preserves the original, measured values. Any such interpolation technique will however also preserve the non-uniform sampling inherent in our data structure. High frequency details will only be available along the laser lines and yield noticeable artifacts. Figure 4 (b) shows a reconstruction result of the push-pull algorithm. The lines on which the original densities have been sampled can still be seen going from left to right.

2.4.2. *Approximation*

We therefore opted for a more general reconstruction approach that approximates the sample values and yields a smoother reconstruction. We formulate our approximation problem as follows: Given are n discrete samples of measured density values $D(\mathbf{p}_i)$ at locations $\mathbf{p}_i$ $(i = 0,\ldots,n-1)$ on the laser lines. We then approximate the field at a position $\mathbf{r}$ as

$$\widetilde{D}(\mathbf{r}) = \frac{\sum_{i=0}^{n-1} D(\mathbf{p}_i)\cdot w(\|\mathbf{r}-\mathbf{p}_i\|)}{\sum_{i=0}^{n-1} w(\|\mathbf{r}-\mathbf{p}_i\|)}. \tag{11}$$

The weighting function w is defined as

$$w(x) = \begin{cases} 0.5\cdot\cos(\frac{x\cdot\pi}{R})+0.5 & \text{for } x < R \\ 0 & \text{else} \end{cases}. \tag{12}$$

The parameter R which determines the width of the reconstruction kernel needs to be manually selected for a given sampling configuration. Note that R has to be chosen such that in the R-neighborhood of every point $\mathbf{r}$ of the domain there is at least one sample point $\mathbf{p}_i$. Figure 4 (c) shows a result of this reconstruction approach. It looks much more smooth and lacks the artifacts due to the irregular sampling of the original volume.

3. Simulation

To perform an analysis of a dataset with ground truth we used a 100 frame simulation of smoke emitted from the border of a volume using the technique of Treuille et al. [11]. The data was stored as a 64^3 voxel density field. Assuming that each dataset is defined over the domain $[0,1]^3$ and assuming a trilinear interpolation between the grid points, we have continuous scalar fields f_g for each time frame which act as ground truth.

In order to reconstruct one scalar field, we consider a bundle of 100 rays starting from $(\frac{1}{2},\frac{1}{2},-3)$ and passing through $(\frac{i}{9},\frac{j}{9},1)$ for $i,j = 0,\ldots,9$. Then we sampled f_g in its domain along the rays and apply our approximation technique with parameter $R = 8$ to get a reconstructed field $f_1^{R=8}$. In a second test, we add a second bundle of 100 rays starting at $(-5,\frac{1}{2},\frac{1}{2})$ and passing through $(1,\frac{i}{9},\frac{j}{9})$ for $i,j = 0,\ldots,9$. The field reconstructed from these 200 rays with $R = 8$ is $f_2^{R=8}$. Figure 3 shows $f_g, f_1^{R=8}$, and $f_2^{R=8}$ for Frame 60 of the dataset. While both reconstructions faithfully represent the overall structure of the field, it is clear that many high-frequency details are lost. We therefore computed a smoothed version of the ground truth field by convolving it with a normalized version of the reconstruction kernel w (Equation 12). Figure 3(d) depicts the smoothed ground truth field $f_g^{R=8}$ for a kernel radius $R = 8$ which is well approximated by both, $f_1^{R=8}$ and $f_2^{R=8}$.

For comparison, we also used the push-pull algorithm described in Section 2.4.1 on the same dataset. For the reconstruction, we sampled each volume with 2 bundles of 100 rays as before so that both reconstruction algorithms work on the same input data. We show the interpolation result using the push-pull algorithm for Frame 60 of the dataset (f_2^{pp}) in Figure 4(b). The result is not so smooth as $f_2^{R=8}$ for the same frame shown in Figure 4(c). The lines on which the volume has been sampled can be still be seen as horizontal artifacts.

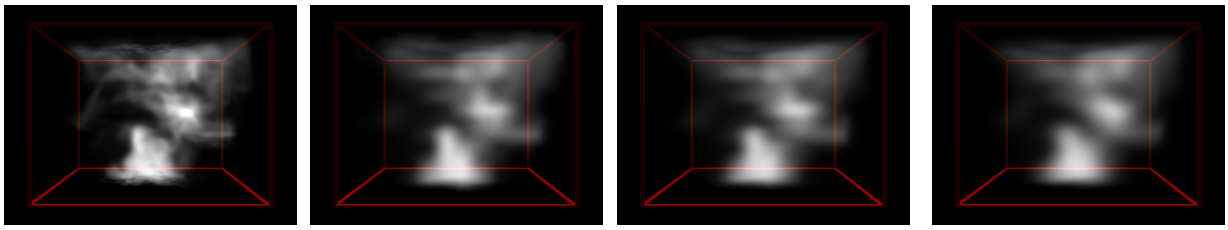

(a) ground truth f_g

(b) reconstruction $f_1^{R=8}$ using one bundle of 10×10 rays

(c) reconstruction $f_2^{R=8}$ using two bundles of 10×10 rays

(d) smoothed ground truth $f_g^{R=8}$

Fig. 3. Result for the simulated smoke dataset. *(a):* Rendering of Frame 60 of the synthetic smoke dataset. *(b) and (c):* Reconstruction using one bundle and two bundles of 10×10 rays, respectively, and $R=8$. *(d):* Rendering of the smoothed original volume with $R=8$.

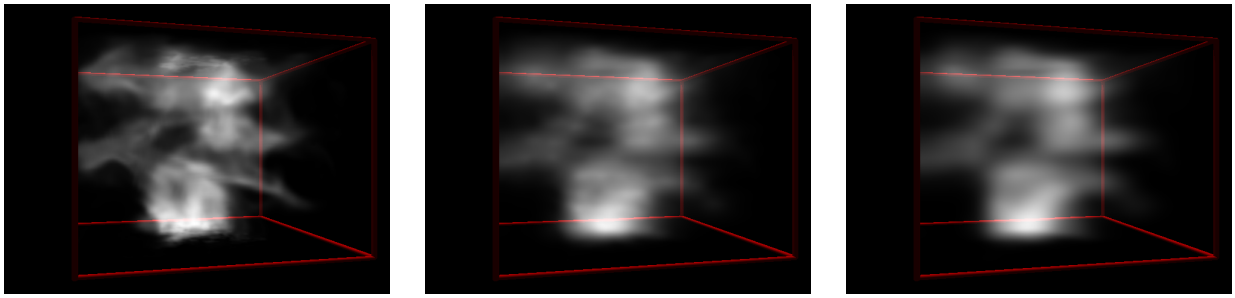

(a) ground truth f_g

(b) interpolation f_2^{pp} using the push-pull algorithm with 2 bundles of 10×10 rays

(c) approximation $f_2^{R=8}$ using 2 bundles of 10×10 rays

Fig. 4. Frame 60 of the synthetic smoke dataset, rotated by 75 degrees. *(a):* Ground truth. *(b) and (c):* Reconstruction using the push-pull algorithm and our approximation technique. Note the line artifacts in the interpolated result f_2^{pp}.

3.1. *Error Analysis*

We define the RMS error between two scalar fields f and f' stored as a voxel densities sampled at a set of identical locations $\mathbf{V}$ as

$$\mathrm{RMS}(f,f') = \sqrt{\frac{\sum_{v_i\in\mathbf{V}}(f(v_i)-f'(v_i))^2}{\|\mathbf{V}\|}}. \qquad (13)$$

In practice, $\mathbf{V}$ corresponds to the set of 64^3 voxels defining our field. Figure 5 depicts the RMS error between various versions of the field for all 100 frames in the dataset. The density values in the original dataset vary between 0 and 1.6.

The RMS errors between the ground truth f_g and the reconstructions from one and two ray bundles ($f_1^{R=8}$ and $f_2^{R=8}$) are almost identical. The RMS error decreases drastically when it is computed against the smoothed version of the ground truth $f_g^{R=8}$. Furthermore, the reconstruction from two ray bundles $f_2^{R=8}$ compares now much better than the reconstruction from a single ray bundle $f_1^{R=8}$. This suggests that most of the error in the reconstructions is due to the sparse sampling and smooth approximation that suppresses high frequency detail. To verify this, we computed the RMS error $\mathrm{RMS}(f_g, f_g^{R=8})$ between the ground truth field and the smoothed version of the ground truth field. Figure 5 shows that this error is only slightly lower than $\mathrm{RMS}(f_g, f_2^{R=8})$, i.e., most of the reconstruction error seems to be due to the loss of high frequency detail.

Figure 6 shows the RMS error for the approximation technique and the interpolation using the push-pull algorithm. The error produced by the push-pull interpolation is lower than that of the reconstruction throughout the whole dataset. This might be an indication that the push-pull algorithm does a better job reconstructing the high-frequency detail.

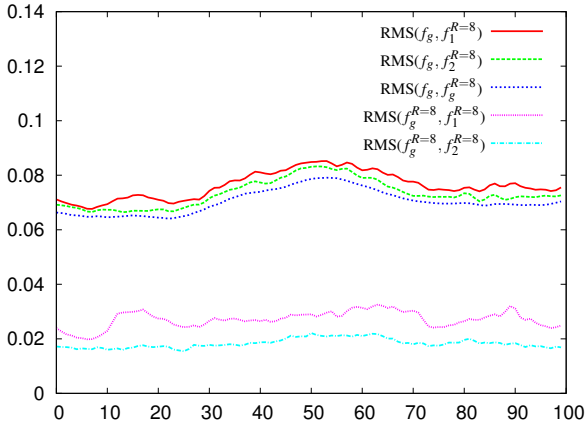

Fig. 5. Various RMS errors for the 100 frames contained in the simulated dataset. Horizontal axis: frame number. Vertical axis: RMS error. The density values in the original dataset vary between 0 and 1.6. The first two lines show the RMS error between ground truth f_g and the reconstruction using 1 and 2 bundles of laser rays, RMS($f_g, f_1^{R=8}$) and RMS($f_g, f_2^{R=8}$), respectively. The third line represents the RMS error between ground truth and a version of the ground truth which has been smoothed using the same kernel that is used in the reconstruction (RMS($f_g, f_g^{R=8}$), Equation 12). The two lines on the bottom of the graph show the RMS error between the smoothed ground truth and the reconstruction using 1 and 2 bundles of laser rays RMS($f_g^{R=8}, f_1^{R=8}$) and RMS($f_g^{R=8}, f_2^{R=8}$), respectively.

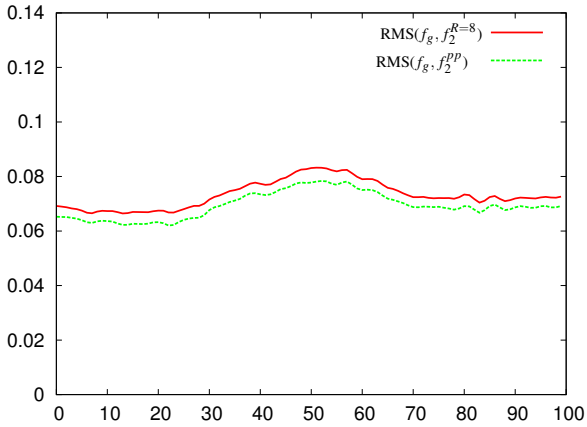

Fig. 6. Comparison of the RMS errors from different reconstruction techniques for the 100 frames contained in the simulated dataset. The approximation was computed using 2 bundles of laser rays (RMS($f_2^{R=8}$)). The error for the push-pull algorithm is shown by RMS(f_2^{pp}). Horizontal axis: frame number. Vertical axis: RMS error.

4. Acquisition System

We built a prototype of an acquisition system to test our ideas in practice. The setup contains two collimated laser sources – a 130 mW red laser and a 30 mW blue laser. Each collimated laser beam is transformed into a bundle of perspective rays using a burst grating. A black mask limits the number of rays in each bundle to 5×5 rays for each laser. The generated ray bundles are roughly perpendicular to each other; their intersection defines a measurement volume of about $50\times24\times50$ cm^3 (see Figure 2, right, for an image of the measurement setup). We use a smoke machine to create a spatially varying density of scattering media.

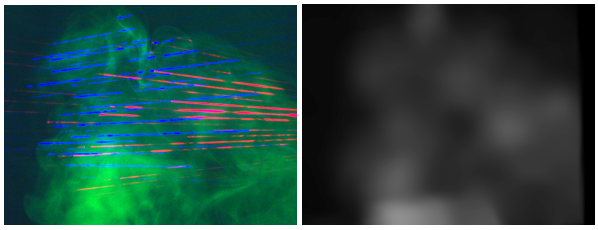

Fig. 7. Acquired image of smoke and reconstructed density field. *Left:* Input image with two independent grids of laser lines (red, blue) sampling the volume and diffuse green illumination (image intensity rescaled for display). *Right:* Density field reconstructed from this single image.

A high quality color CCD camera is used to capture images of the measurement volume. Its placement ensures that no two rays of the same color project to the same location on the image plane. We are thus able to capture the two bundles independently using the camera's red and blue channel. In addition, we illuminate the measurement volume diffusely with green LEDs and use the green channel of the camera to capture simultaneously a ground truth image of the acquired dataset. Figure 7, left, shows an example input image of the system. Although all three light sources have a narrow spectral response, we observe crosstalk between the two lasers which we remove using standard image processing techniques.

4.1. *Calibration and Capture*

For geometric calibration of the camera and the lasers we capture several high-dynamic range images [12] of each bundle of laser rays illuminating a yellow and white checkerboard pattern. This allows us to reliably detect the corners of the calibration pattern as well as the centers of the laser spots. After computing the 3D location of these spots using a calibration toolbox [13] we can estimate the position of the laser lines in space relative to the camera. Figure 8 (left) shows a visualization of the spatial sampling in which the two bundles of laser rays are clearly visible. Using the calibration data, we can now extract samples $I_{\mathbf{p}}$ from the camera images by marching densely along the projections of

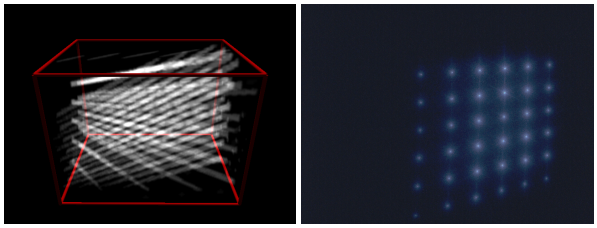

Fig. 8. Geometric and photometric calibration of the setup. *Left:* Visualization of the spatial sampling. The two bundles of laser rays are clearly visible. *Right:* Calibration image for the blue laser to recover the relative intensities I_{l_i} for the individual rays (tone-mapped).

the rays and taking a sample at each step. As noted in Section 2.2, we need to ensure that the full width of the projected laser line is captured. We therefore integrate the contributions to $I_{\mathbf{p}}$ along a small line segment perpendicular to the projected ray direction. We then low-pass filter and downsample the obtained intensity samples along each ray in order to reduce noise and facilitate further processing, yielding about 150 samples per ray.

The burst gratings create bundles of rays where each laser line can have a different intensity. We therefore need to recover the relative intensity I_{l_i} of all laser lines in each bundle in the calibration phase. To this end, we capture a high-dynamic range image per laser of a sheet of subsurface scattering plastics [2] illuminated by the corresponding ray bundle (see Figure 8 right). We integrate the laser intensity over a constant area around each laser spot to get I_{l_i}. The two lasers might still behave differently, e.g., due to different scattering properties for different wavelengths. In a subsequent calibration step, we therefore capture images of smoke and recover separate density fields D_{red} and D_{blue} for the red resp. the blue laser bundle. We then determine a scale factor k that minimizes the RMS error between D_{red} and $k \cdot D_{\text{blue}}$ and scale the input data for the blue channel accordingly before reconstructing the density field.

4.2. *Acquisition Results*

We captured several datasets with the acquisition system described in Section 4 and depicted in Figure 2 (right). All images were taken with 0.25 s exposure time. Captured results are shown in Figures 7 and 9. The results are rendered using a raytracing-based direct volume rendering approach.

[2] The subsurface scattering material spreads out the laser intensity over a greater area. Thereby the dynamic range of intensity that has to be measured is reduced.

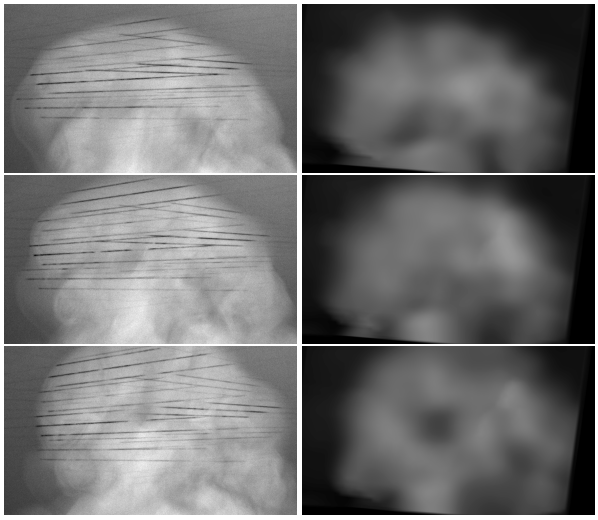

Fig. 9. Results for smoke from a smoke machine. The three images were taken in sequence from top to bottom. The images on the left show ground truth photographs of the scene extracted from the green channel. The images on the right show renderings of our reconstruction.

Figure 7 shows an input image capturing smoke from a smoke machine. The intensity variations along the laser lines are clearly visible. In addition, the blue laser lines are brighter and tighter focused than the red lines. This is corrected by integrating over the width of the laser line (Section 4.1 and by the intensity scaling described in Section 4). In the result image on the right, note, how much detail could be reconstructed from this single input view.

Figure 9 shows comparisons between ground truth photographs and renderings for three images of dataset consisting of 50 images captured at approximately 3 fps. Note that the speed is mainly constrained by the frame rate of the camera and not by the measurement principle. The ground truth photographs were extracted from the camera's green channel as described in Section 4. The reconstructed dataset captured the overall shape of the smoke as well as prominent features. Its resolution is, however, limited due to the sparse sampling using only 5×5 grids of laser lines.

5. Discussion

We presented a new approach to sample dynamic volumetric density fields using grids of laser lines as illumination. This allows us to continuously sample in

the time domain at the cost of sparser sampling on the spatial domain.

Like other measurement systems such as Hawkins et al. [4] or Narasimhan et al. [14], we are assuming that the scattering behavior inside the measurement volume is dominated by single scattering. This limits both, the size of the measurement volume and the density of the scatterer inside the volume, due to two effects: First, the intensity of the laser rays I_{l_i} and the scattered intensity $I_{\mathbf{p}}$ decrease inside the measurement volume due to outscattering and absorption yielding a systematic bias in the reconstructed field $D(\mathbf{r})$. Modeling and inverting this effect for spatially varying densities is difficult even if all scattering parameters are known.

Second, as the diffuse intensity I_{d} increases, the signal-to-noise ratio for the measurement of the directly scattered intensity decreases significantly. This is a fundamental problem to all approaches of this kind which can be only partially compensated for, e.g., by subtracting the diffuse illumination [4]. Narasimhan et al. [15] recognized this problem and solve it by avoiding multiple scattering in the first place. They dilute their working medium until single scattering clearly dominates its scattering behavior.

6. Future Work

There are several directions for further research improving both the acquisition setup and the reconstruction of the complete density field.

A different camera system would allow us to operate the whole setup at a higher frame rate removing motion blur from captured images.

The properties of the gratings that are used to generate the ray bundles have a great impact on the size of the volume that can be effectively measured and on the number of lines that can be used. The rapid decrease in intensity for the outer lines of the grid imposes a strong limit on the number of useful rays. The angle between individual lines of the grid limits the size of the volume which can be sampled at a certain spatial sampling rate. All these properties do not only depend on the grating itself, but also on the wavelength of the laser source. Thus, the gratings have to be carefully chosen to match an existing laser.

Due to all these problems it might be preferable to use individual laser sources (e.g., a set of laser pointers) to generate the lines independently instead of a single laser and a grating. This would allow a much denser sampling grid. The number of laser lines is then only limited by their projected width in the captured image. It could also greatly facilitate the setup of the whole system, since an occluded line could be moved independently until it is visible. Furthermore it would minimize the need for a calibration of the intensities.

The current data processing approach makes no assumption about the structure of the density field $D(\mathbf{r})$ and yields therefore a smooth reconstruction of the smoke volume (especially in sparsely sampled dimensions). Reconstruction algorithms that make use of prior knowledge of the structure of the data (e.g., [16]) can improve the visual quality of the reconstructed density field. Alternatively, the structure could be inferred by analyzing the frequency content in denser sampled dimensions in the spirit of Dischler et al. [17].

Acknowledgements

We would like to thank Adrian Treuille for providing the simulated smoke dataset. This work was supported in part by a Feodor Lynen Fellowship granted by the Alexander von Humboldt Foundation, the University of Washington Animation Research Labs, Adobe, and Microsoft.

References

[1] S. W. Hasinoff, K. N. Kutulakos, Photo-Consistent 3D Fire by Flame-Sheet Decomposition, in: International Conference on Computer Vision, 2003, pp. 1184–1191.

[2] I. Ihrke, M. Magnor, Image-Based Tomographic Reconstruction of Flames, in: ACM Siggraph / Eurographics Symposium on Computer Animation, 2004, pp. 367–375.

[3] I. Ihrke, M. Magnor, Adaptive Grid Optical Tomography, in: Vision, Video, and Graphics, 2005, pp. 141–148.

[4] T. Hawkins, P. Einarsson, P. Debevec, Acquisition of Time-Varying Participating Media, ACM Transactions on Graphics 24 (3) (2005) 812–815.

[5] B. Yip, J. K. Lam, M. Winter, M. B. Long, Time-Resolved Three-Dimensional Concentration Measurements in a Gas Jet, Science 235 (1987) 1209–1211.

[6] S. Deutsch, T. Dracos, Time Resolved 3D Passive Scalar Concentration-Field Imaging by Laser Induced Fluorescence (LIF) in Moving Liquids, Measurement Science and Technology 12 (2) (2001) 188–200.

[7] C. F. Bohren, D. R. Huffman, Absorption and Scattering of Light by Small Particles, Wiley & Sons, 1983.

[8] A. Ishimaru, Wave Propagation and Scattering in Random Media, Academic Press, 1978.

[9] S. J. Gortler, R. Grzeszczuk, R. Szeliski, M. F. Cohen, The Lumigraph, in: SIGGRAPH 96, 1996, pp. 43–54.

[10] I. Drori, D. Cohen-Or, H. Yeshurun, Fragment-Based Image Completion, ACM Transactions on Graphics 22 (3) (2003) 303–312.

[11] A. Treuille, A. Lewis, Z. Popović, Model Reduction for Real-Time Fluids, ACM Transactions on Graphics 25 (3) (2006) 826–834.
[12] P. Debevec, J. Malik, Recovering High Dynamic Range Radiance Maps from Photographs, in: SIGGRAPH 97, 1997, pp. 369–378.
[13] J.-Y. Bouguet, Camera Calibration Toolbox for MATLAB, http://www.vision.caltech.edu/bouguetj/calib_doc/ (2006).
[14] S. G. Narasimhan, S. K. Nayar, B. Sun, S. J. Koppal, Structured Light in Scattering Media, in: International Conference on Computer Vision, 2005, pp. 420–427.
[15] S. G. Narasimhan, M. Gupta, C. Donner, R. Ramamoorthi, S. K. Nayar, H. W. Jensen, Acquiring Scattering Properties of Participating Media by Dilution, ACM Transactions on Graphics 25 (3) (2006) 1003–1012.
[16] S. Owada, F. Nielsen, M. Okabe, T. Igarashi, Volumetric Illustration: Designing 3D Models with Internal Textures, ACM Transactions on Graphics 23 (3) (2004) 322–328.
[17] J.-M. Dischler, D. Ghazanfarpour, R. Freydier, Anisotropic Solid Texture Synthesis Using Orthogonal 2D Views, Computer Graphics Forum 17 (3) (1998) 87–96.